Carvalho, B.B., et al., 2023, **Revealing the link between A-type granites and hottest melts from residual metasedimentary crust:** Geology, v. XX, p. XXX–XXX, https://doi.org/10.1130/G51097.1

Supplemental Material

Further information on the geological background, petrography, and methods.

Tables S1–S4. Major element composition of garnet and sapphirine, and major element and trace element analyses of melt inclusions and Zr contents of rutile.

GSA Supplemental Material

Carvalho et al.: Revealing the link between A-type granites and hottest melts from residual metasedimentary crust.

1. Geological background

The Lützow-Holm Complex (LHC) is a high-grade terrane in eastern Dronning Maud Land of East Antarctica, where metamorphic conditions related to the Pan-African event increase from amphibolite-facies to granulite-facies (Hiroi et al., 1991). The LHC is composed of various felsic and mafic gneisses and granulites of sedimentary and igneous origin along with syntectonic and late-tectonic intrusive rocks. A clockwise P–T path has been proposed due to the presence of 1) relict prograde kyanite and staurolite inclusions within garnet and plagioclase in pelitic gneisses where sillimanite is stable and ubiquitous (Hiroi et al., 1994; Kawakami and Motoyoshi 2004; Satish-Kumar et al., 2006), 2) hornblende, spinel and sapphirine inclusion in garnet from ultramafic granulites, 3) replacement of garnet by symplectites of orthopyroxene, anorthite and spinel (Hiroi et al., 1991), and 4) the occurrence of retrograde andalusite in rocks that contained sillimanite at the peak of metamorphism (Hiroi et al., 1983; Kawakami et al., 2008).

The Rundvågshetta area (this study), is located within the thermal maximum of the LHC, where ultrahigh temperature (UHT) conditions were reached (Motoyoshi and Ishikawa 1997; Kawakami and Motoyoshi 2004; Kawasaki and Motoyoshi 2006; Yoshimura et al., 2008). The metamorphic basement comprises pelitic, mafic and intermediate gneisses, subordinate pegmatites, ultramafic and calc-silicate rocks (Motoyoshi et al., 1986). Mineral assemblages consistent with UHT conditions in this area include spinel + quartz (Motoyoshi et al., 1985), orthopyroxene + sillimanite + quartz (Kawasaki et al., 1993), sapphirine + quartz (Yoshimura et al., 2008; Durgalakshmi et al., 2021) and osumilite (Kawasaki et al., 2011). Several approaches have been adopted to estimate the peak *P–T* conditions attained in the area. Investigation of petrogenetic grids

and garnet-orthopyroxene geothermometry on pelitic granulites indicated a thermal peak of 1000°C at 11 kbar (Motoyoshi and Ishikawa, 1997). Even higher temperatures were obtained by experimental petrology applied to the sillimanite-cordierite-sapphirine bearing granulites, with estimated P-T conditions of 925-1039°C and 11.5-15 kbar for metamorphic peak and 824-1010°C and 6-10 kbar for post peak evolution (Kawasaki and Motoyoshi, 2006). Using the peak assemblages sapphirine + quartz and orthopyroxene + sillimanite + quartz, Yoshimura et al. (2008) inferred conditions of 1000-1100°C at 10-12 kbar. By means of phase equilibria modelling, Durgalakshmi et al. (2021) proposed instead that peak conditions at Rundvågshetta up to 1040°C slightly above 8 kbar were followed by an isobaric cooling down to 920°C and subsequently isothermal decompression <8 kbar. Suzuki and Kawakami (2019) applied Zr-in-rutile thermometer to the garnet-sillimanite gneiss without any diagnostic UHT mineral assemblage and obtained high-T condition of 850 ± 15 °C/0.1 kbar to 927 ± 16 °C/12.5 kbar.

Pioneering reconnaissance-scale U–Pb zircons dating by SHRIMP (Shiraishi et al., 1992; Shiraishi et al., 1994) indicated an Early Paleaozoic age (Cambrian 521 ± 9 Ma and 553 ± 6 Ma) for the metamorphism of the LHC, with progressively younger ages with increasing metamorphic grade. Zircons from a garnet-rich quartzo-feldspatic gneiss from Rundvågshetta provided discordant Late Archean to Early Proterozoic (2900 to 1500 Ma) ages in inherited grains, whereas the UHT event was recorded by a younger 521 ± 9 Ma Paleozoic age. Such data were the first strong evidence for the correlation of the LHC with the Pan-African mobile belts in Sri Lanka and Africa, hence revealing those as fundamental areas to investigate the evolution of the Gondwana supercontinent (Shiraishi et al. 1992; Shiraishi et al. 1994; Yoshimura et al. 2008). Two schools of thought debate whether the LHC underwent a single long-lived orogenic event between >600 Ma and 520 Ma (Dunkley et al., 2014) or polymetamorphic events, i.e., Ky-grade metamorphism at 650–580 Ma and Ky-Sil grade metamorphism 560–500 Ma (Kawakami et al., 2016). We refer the reader to Dunkley et al. (2020) for a complete summary of the current available U-Pb ages for the LHC.

A recent thorough geochronological investigation of sapphirine-quartz-bearing Mg-Al granulites from Rundvågshetta revealed that the peak of UHT metamorphism, under conditions of 1020-1040°C and 8 kbar, occurred at 554 ± 4.7 Ma (Durgalakshmi et al., 2021). Outer overgrowths of zircon yielded younger ages at 530.8 ±4.7 Ma, which were then interpreted to mark the cooling and retrograde evolution of the terrane. An important outcome of this work is that zircon was stable throughout the whole metamorphic history, surviving UHT conditions.

2. Additional petrographic information

The sample selected for the melt inclusion study (69°54'12.84"S; 39°3'15.23"E) is a coarse-grained heterogeneous metapelitic granulite, comprising predominant mafic domain and a volumetrically smaller relatively more felsic domain (see Figure 1A in the main text).

The mineral association in the mafic domain typically contains orthopyroxene (Al_2O_3 6-8.8 wt.%) + sillimanite + quartz + zoned garnet ($Prp_{42-55}Alm_{40-52}Gr_{3-4}Sp_{0.2-1}$; XMg 0.5) + K-feldspar + cordierite (XMg 0.86) + rutile ± sapphirine ± biotite (X_{Mg} 0.75; TiO_2 3.7-6.3 wt.%) ± plagioclase (An_{35-46}). The mafic domain has garnet rimmed by post-peak symplectites of cordierite, orthopyroxene and sapphirine.

In contrast, the more felsic, melt-rich domain is composed of mesoperthite + quartz + garnet + sillimanite + brown biotite (X_{Mg} 0.7; TiO_2 3.7-5.4 wt.%) + rutile ± cordierite, but is free of orthopyroxene. Accessory phases in the matrix are zircon and monazite. Garnet porphyroblasts (0.2-0.8 cm) in the melt-rich domains are more magnesian ($Prp_{54-57}Alm_{39-42}Gr_{3-4}Sp_{0.2-0.6}$, X_{Mg} 0.57) and contain clusters of glassy inclusions and crystallized melt inclusions (nanogranitoids) together with multiphase fluid inclusions and accessory phases (mainly rutile and apatite). Composite inclusions of sapphirine + quartz may also be found in these garnets. The more magnesian composition of garnet probably results from the contrasting X_{Mg} between the different domains as they have different coexisting ferromagnesian phases (orthopyroxene, sapphirine and cordierite in the mafic domains, and mostly biotite in the melt-rich domains). Commonly present K-feldspar

(mesoperthite) is coarse-grained, subhedral and together with quartz, may form leucocratic patches which are interpreted as in-source leucosomes (e.g. Sawyer, 2008).

3. Materials and analytical methods

Sampling: Rock samples investigated in this study were collected during the expedition JARE-46 (Japanese Antarctic Research Expedition, years 2004-2005), and were supported by the National Institute of Polar Research (NIPR) under Ministry of Education, Culture, Sports, Science and Technology (MEXT), Japan.

FESEM: Backscattered-electron (BSE) images of the inclusions were obtained using a Sigma Zeiss field-emission scanning electron microscope (FESEM) equipped with an Oxford XMax EDS Silicon Drifted detector at the CNR–IENI, Padova. Images were acquired commonly using 8–15 kV accelerating voltages at various magnifications and the compositional X-ray maps were acquired at 20–15 kV.

Microprobe: Major element compositions in minerals and glassy inclusions were analysed using a JEOL JXA 8200 Superprobe at the Dipartimento di Scienze della Terra, Università di Milano, Italy. The operating conditions for analyses of minerals were 20 nA beam current, 20kV acceleration voltage, and 1 μm beam diameter, with counting times of 10s on peak and 5s on background. The composition of glassy inclusions was determined using 15 kV accelerating voltage, 5 nA beam current, 10 s on the peak and 5 s background, and 1 μm beam diameter to avoid contamination from the surrounding host. Alkali loss was estimated using leucogranitic standards showing a similar composition to the melts, and correction factors were applied for Na, K, Al and Si. The standard used was the anhydrous glass B from Morgan and London (2005). Representative microprobe analyses of minerals are given in Supplementary Table DR1, and the composition of melt inclusions

is given in Supplementary Table DR2. The Fe^{3+} contents of sapphirine were estimated using the stoichiometric method of Droop (1987).

LA-ICPMS: Trace element analyses of glassy inclusions, nanogranitoids, host garnets, and rutile were performed on 60 µm, doubly-polished, thick sections using a quadrupole-based Thermo Fisher Scientific iCAP-Q ICP-MS coupled with a Teledyne / Photon Machine G2 excimer laser (193 nm) equipped with a Two-Volume HelEx 2 cell at the Department of Physics and Geology, University of Perugia. Helium was utilized as a carrier gas. The helium carrier exiting the ablation cell was mixed with a mixture of nitrogen and argon make-up gas before entering the ICP torch to enhance the sensitivity and maintain stable excitation conditions, respectively. The LA-ICP-MS system was optimized for dry plasma conditions before each analytical session on a continuous linear ablation of the NIST SRM612 glass standard reference material by maximizing the signals for selected masses (La^+ and Th^+), minimizing oxide formation by reducing the ThO^+/Th^+ ratio below 0.5%, and maintaining the U^+/Th^+ ratio close to 1. All measurements were carried out using time-resolved analysis of ~30 s of measuring the instrumental background, i.e., analysis of the carrier gas with no laser ablation, followed by ~60–100 s of data acquisition with the laser firing on the sample surface, and 30 s of washout. The laser-beam diameter, the repetition rate, and the laser energy density on the sample surface were 12-25 µm (12 µm for melt inclusions and few rutile grains included in garnet and 25 µm for rutile in garnet and in the matrix), 8 Hz, and ~3.5 J/cm^2, respectively. Data reduction has been performed by Iolite4 (Paton et al., 2011) using the standard reference glass NIST610 and BCR2G reference material as calibrator and quality control (secondary standard), respectively. The SiO_2 measured by EPMA has been utilized as internal standards for melt inclusions and garnet. The internal standard for rutile was TiO_2. Separate experiments have been carried out for the different spot-sizes to limit fractionation effects (e.g., Petrelli et al., 2016). To note, when it is possible to use larger spot sizes, it improves the precision, accuracy and the detection limit of analysis (e.g., Petrelli et al., 2016). The figure of merits for the different spot-sizes utilized in the present study have been

investigated in Petrelli et al. (2016) and checked on the BCR2G reference material (reported in their supplementary material). Nonetheless, at beam sizes larger than 15 μm, precision and accuracy are equal or better than 10%. At smaller beam sizes, i.e., 12 μm, precision and accuracy are still of the order or better than 10% for concentrations above ~1.5 μg g^{-1} (Petrelli et al., 2016). The data reduction strategy adopted for melt inclusions, that are mostly unexposed, are based on the protocol described by Halter et al. (2002) and are thoroughly described in Ferrando et al. (2019). It consists of a two-step procedure (Halter et al., 2002). In detail, during the first step, we determined the cumulative host plus melt inclusion content. Then, trace-element compositions of melt inclusions were estimated by correcting the cumulative host plus melt inclusion values for the contribution of the host mineral (Halter et al., 2002). The error propagation has been modelled using a Monte-Carlo approach in agreement with Ferrando et al. (2019). To note, elements strongly compatible in the host garnet (e.g., HREE and Y) have not been determined in the melt inclusions due to their dominance of the cumulative host plus melt inclusion signals and derived concentrations, resulting in unacceptable error values for melt inclusions after the error propagation. Trace analyses of melt inclusions are given in Supplementary Table DR3, and the composition of rutile is given in Supplementary Table DR4.

H_2O contents of the melts: The H_2O contents of glassy inclusions was estimated as the difference to 100% from the electron microprobe total (Table DR2), but also determined by laser Raman microspectroscopy using the method of Thomas et al. (2006). Raman spectra of unexposed glassy inclusions (at depths < 10μm) and standard glasses of known H_2O contents (DL Core and DL Sand – Acosta-Vigil et al., 2003; LGB - Behrens and Jantos, 2001) were collected in the range 3100-3800 cm^{-1}, with an integration time of 50 seconds and five accumulations. Micro-Raman measurements were performed on doubly-polished thick sections at the Experimental Mineralogy Lab, Department of Earth and Environmental Sciences, University of Pavia, Italy, using a HORIBA LabRam HR Evolution with frequency-doubled Nd:YAG laser with 532 nm/100 mW excitation wavelength and

holographic gratings of 600 grooves/mm. A petrographic microscope Olympus (100x objective) was used to focus the laser on the selected inclusions. Data were processed using *LabSpec 6.* Raman spectra of the standard glasses and the obtained calibration curves are presented in Figure DR1. The calibration curve used in presented in Figure DR1c.

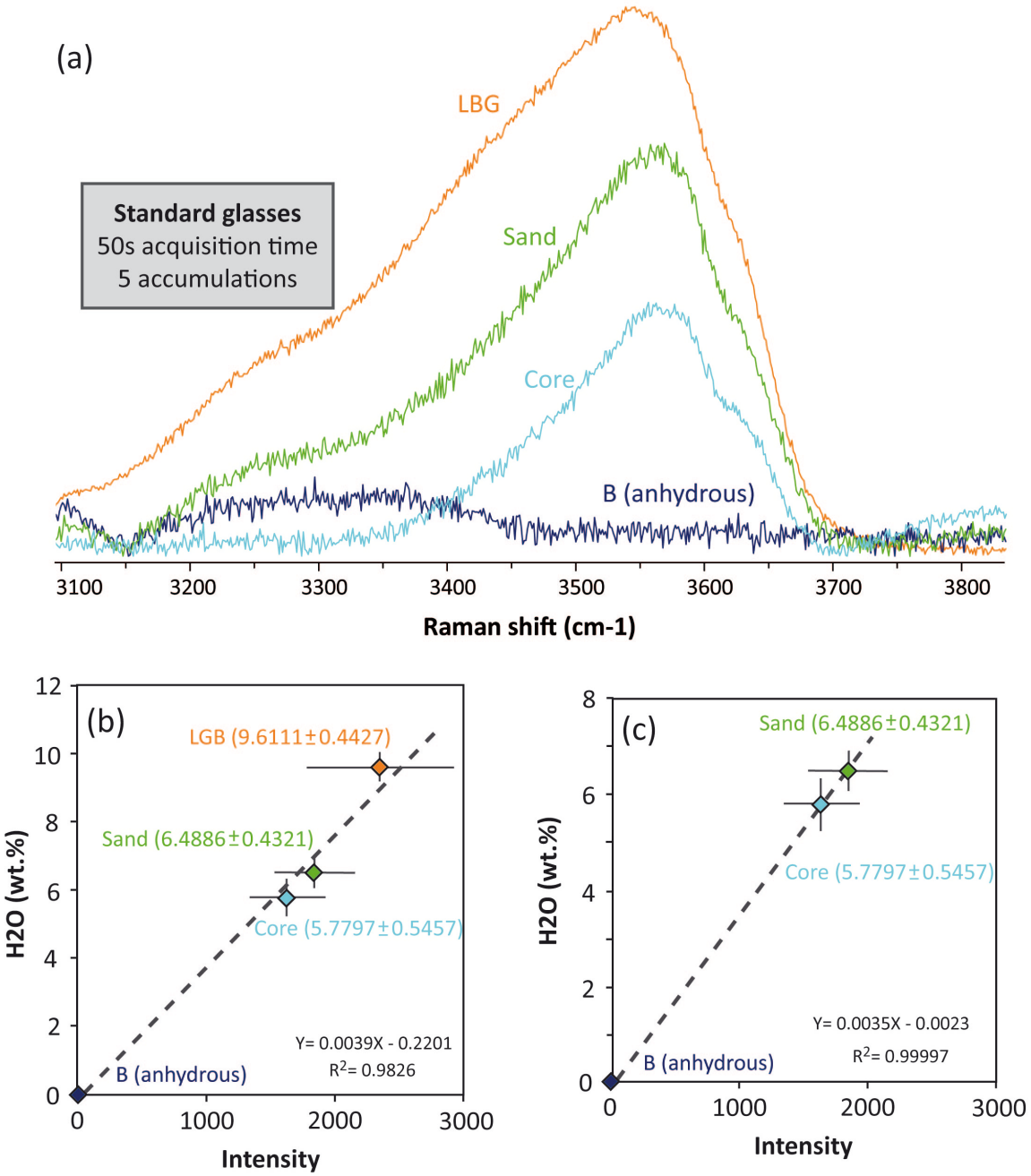

Supplementary Figure DR1: (a) Raman spectra of standard glasses with different H_2O contents. (b) Calibration curve for H_2O considering the intensity of the asymmetric OH- band at 3555 cm^{-1}

measured on standard glasses LGB, Sand, Core and B (method of Thomas et al., 2006). (c) Calibration curve for H_2O considering the intensity of the asymmetric OH- band at 3555 cm^{-1} measured on standard glasses Sand, Core and B; this is the one used in the present study.

Phase equilibria modelling: Mg–Al ultrahigh temperature rocks are generally microstructurally and mineralogically complex and modelling their phase equilibria can be very tricky and often demands the use of compositions of local domains (Kelsey and Hand, 2015). Here, we are interested in finding the P–T conditions of formation of melt inclusion-bearing garnet, which are thought to be related to the second melting event, occurred at ca. 550-530 Ma (Durgalakshmi et al., 2021). The local bulk composition of a rock slice made of 90% mafic and 10% felsic domain was obtained from XRF analysis. Phase equilibria modelling was performed in the Na_2O–CaO–K_2O–FeO–MgO–Al_2O_3–SiO_2–H_2O–TiO_2–Fe_2O_3 (NCKFMASHTO) system, using Perple_X software (Connolly, 2009) with the internally consistent data set ds62 (Holland and Powell, 2011). Values of H_2O and Fe_2O_3 were selected calculating T–X diagrams at 8.5 kbar, following the procedure described in Korhonen et al. (2013). The H_2O was selected so that the stable assemblage is present just above the solidus (i.e. the observed phase assemblage is in equilibrium with the last remnants of melt). A total of 12% Fe as Fe^{3+} was selected, because it is appropriate to reproduce the observed assemblage. Notably, such a value of ferric iron is in agreement with those determined by Fe^{2+} titration on rutile-, ilmenite-bearing UHT metapelites (Korhonen et al., 2014). The final composition used for the modelling (mol. %) is: 57.21 SiO_2, 1.86 TiO_2, 10.74 Al_2O_3, 8.18 FeO, 16.98 MgO, 1.04 CaO, 0.67 Na_2O, 2.59 K_2O, 0.32 H_2O, 0.44 O_2. The following a–*x* relations were selected: melt, garnet, orthopyroxene, muscovite, biotite, cordierite and magnetite from White et al. (2014a, b), ilmenite from White et al. (2000), plagioclase and K-feldspar from Holland and Powell (2003) and sapphirine from Wheller and Powell (2014). Pure phases included quartz, rutile, kyanite, sillimanite and aqueous fluid. The complete *P–T* pseudosection is reported in Supplementary Figure DR2.

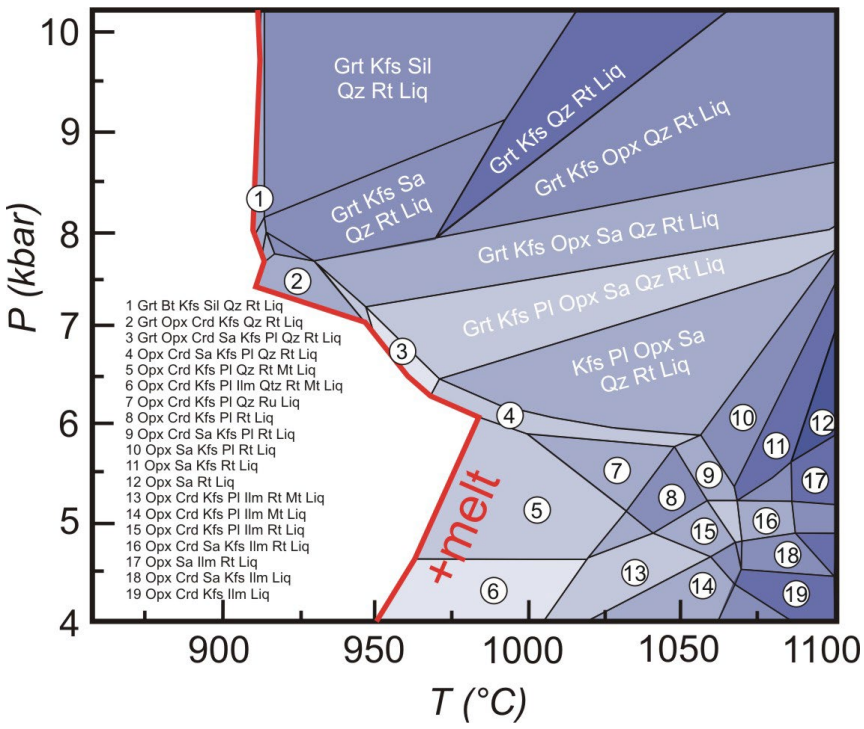

Supplementary Figure DR2: Calculated *P–T* pseudosection for the Rundvågshetta granulite investigated in this study. The red line is the solidus.

Geochemical modeling: melt evolution was modeled by equations of Rayleigh fractionation and bulk cumulation. A range of published end-member solid-melt partition coefficients were used to create bracketing models. In particular, the bulk D values are: 0.44–1.75 for D_{Rb}, 7.61–26-04 for D_{Sr} and 3.51–17.79 for D_{Ba} [single partition coefficients from Ewart and Griffin (1994), Nash and Crecraft (1985), Icenhower and London (1996)]. Crystallizing minerals are K-feldspar and plagioclase (70:30). Additional mixing model was performed by mass balance considering as final endmembers the average MIs and a mafic component (Naumann and Geist, 1999).

References

Acosta-Vigil, A., London, D., Morgan, G. B., and Dewers, T. A., 2003, Solubility of excess alumina in hydrous granitic melts in equilibrium with peraluminous minerals at 700–800 C and 200 MPa, and applications of the aluminum saturation index. Contributions to Mineralogy and Petrology, v. 146, p. 100-119.

Behrens, H. and Jantos, N., 2001, The effect of anhydrous composition on water solubility in granitic melts. American Mineralogist v. 86, p. 14-20.

Connolly, J. A. D., 2009, The geodynamic equation of state: what and how. Geochemistry, geophysics, geosystems, v. 10.

Droop, G., 1987, A general equation for estimating Fe^{3+} concentrations in ferromagnesian silicates and oxides from microprobe analyses, using stoichiometric criteria. Mineralogical Magazine, v. 51, p. 431-435.

Dunkley, D. J., Hokada, T., Shiraishi, K., Hiroi, Y., Nogi, Y., and Motoyoshi, Y., 2020, Geological subdivision of the Lützow–Holm Complex in East Antarctica: from the Neoarchean to the Neoproterozoic. Polar Science, v. 26, p. 100606.

Dunkley, D. J., Shiraishi, K., Motoyoshi, Y., Tsunogae, T., Miyamoto, T., Hiroi, Y., Carson, C. J., 2014, Deconstructing the Lützow–Holm Complex with zircon geochronology. In Abstract of 7th international SHRIMP workshop program, p. 116-121.

Durgalakshmi, I., Sajeev, K., Williams, I. S., Reddy, D. H., Satish-Kumar, M., Jöns, N., Sanjeewa, P., Vinod, S., George, P. M., 2021, The timing, duration and conditions of UHT metamorphism in remnants of the former eastern Gondwana. Journal of Petrology, v. 62, egab068.

Ewart, A., and Griffin, W. L., 1994, Application of proton-microprobe data to trace-element partitioning in volcanic rocks. Chemical Geology, v. 117, p. 251-284.

Ferrando, S., Petrelli, M., and Frezzotti, M. L., 2019, Gradual and selective trace-element enrichment in slab-released fluids at sub-arc depths. Scientific reports, v. 9, p. 1-9.

Halter, W. E., Pettke, T., Heinrich, C. A. and Rothen-Rutishauser, B., 2002, Major to trace element analysis of melt inclusions by laser-ablation ICP-MS: methods of quantification. Chemical Geology, v. 183, p. 63–86.

Hiroi, Y., Shiraishi, K., Yanai, K., and Kizaki, K., 1983, Aluminum silicates in the Prince Olav and Soya Coasts, East Antarctica.

Hiroi, Y., Shiraishi, K., and Motoyoshi, Y., 1991, Late Proterozoic paired metamorphic complexes in East Antarctica, with spe- cial reference to the tectonic significance of ultramafic rocks. In Geological Evolution of Antarctica (Thomson, M.R.A., Crame, J.A. and Thomson, J.W. Eds.). Cambridge University Press, Cambridge, p. 83- 87.

Hiroi, Y., Ogo, Y., and Namba, K., 1994, Evidence for prograde metamorphic evolution of Sri Lankan pelitic granulites, and implications for the development of continental crust. Precambrian Research, v. 66, p. 245-263.

Holland, T., and Powell, R., 2003, Activity–composition relations for phases in petrological calculations: an asymmetric multicomponent formulation. Contributions to Mineralogy and Petrology, v. 145, p. 492-501.

Holland, T. J. B., and Powell, R., 2011, An improved and extended internally consistent thermodynamic dataset for phases of petrological interest, involving a new equation of state for solids. Journal of metamorphic Geology, v. 29, p. 333-383.

Holness, M. B., and Sawyer, E. W., 2008, On the pseudomorphing of melt-filled pores during the crystallization of migmatites. Journal of Petrology, v. 49, p. 1343-1363.

Icenhower, J., and London, D., 1996, Experimental partitioning of Rb, Cs, Sr, and Ba between alkali feldspar and peraluminous melt. American Mineralogist, v. 81, p. 719-734.

Kawakami, T., Hokada, T., Sakata, S., and Hirata, T., 2016, Possible polymetamorphism and brine infiltration recorded in the garnet-sillimanite gneiss, Skallevikshalsen, Lützow-Holm Complex, east Antarctica. Journal of Mineralogical and Petrological Sciences, v. 111, p. 129–143.

Kawakami, T., and Motoyoshi, Y., 2004, Timing of attainment of the spinel+ quartz coexistence in garnet-sillimanite leucogneiss from Skallevikshalsen, Lützow-Holm Complex, East Antarctica. Journal of Mineralogical and Petrological Sciences, v. 99, p. 311-319.

Kawakami, T., Grew, E. S., Motoyoshi, Y., Shearer, C. K., Ikeda, T., Burger, P. V., and Kusachi, I., 2008, Kornerupine sensu stricto associated with mafic and ultramafic rocks in the Lützow-

Holm Complex at Akarui Point, East Antarctica: what is the source of boron?. Geological Society, London, Special Publications, v. 308, p. 351-375.

Kawasaki, T., Ishikawa, M. and Motoyoshi, Y., 1993, A preliminary report on cordierite-bearing assemblages from Rundvagshetta, Lutzow-Holm Bay, East Antarctica: Evidence For A Decompressional PT path.

Kawasaki, T., and Motoyoshi, Y., 2006, Experimental Constraints on the Decompressional P-T Paths of Rundvågshetta Granulites, Lützow-Holm Complex, East Antarctica. Antarctica. Berlin/Heidelberg: Springer-Verlag, p. 23–36.

Kelsey, D. E., and Hand, M., 2015, On ultrahigh temperature crustal metamorphism: phase equilibria, trace element thermometry, bulk composition, heat sources, timescales and tectonic settings. Geoscience Frontiers, 6, 311-356.

Kohn, M. J., 2020, A refined zirconium-in-rutile thermometer. American Mineralogist: Journal of Earth and Planetary Materials, v. 105, p. 963-971.

Korhonen, F. J., Brown, M., Clark, C., and Bhattacharya, S., 2013, Osumilite–melt interactions in ultrahigh temperature granulites: Phase equilibria modelling and implications for the P–T–t evolution of the Eastern Ghats Province, I ndia. Journal of Metamorphic Geology, v. 31, p. 881-907.

Korhonen, F. J., Clark, C., Brown, M. and Taylor, R. J. M., 2014, Taking the temperature of Earth's hottest crust. Earth and Planetary Science Letters, v. 408, p. 341-354.

Motoyoshi, Y., Matsueda, H., Matsubara, S., Sasaki, K., and Moriwaki, K., 1986, Geological map of Rundvagskollane and Rundvagshetta, Antarctica. Antarct. Geol. Map Ser., Sheet 24, with explanatory text 11 p. Tokyo, Natl Inst. Polar Res.

Motoyoshi Y., and Ishikawa M., 1997, Metamorphic and structural evo- lution of granulites from Rundvagshetta, Lützow-Holm Bay, East Antarctica. In: Ricci CA (ed) The Antarctic region: geological evolution and processes. Terra Antartica Publication, Siena, p. 65–72

Morgan, G. B., Acosta-Vigil, A., and London, D., 2008, Diffusive equilibration between hydrous metaluminous-peraluminous haplogranite liquid couples at 200 MPa (H2O) and alkali transport in granitic liquids. Contributions to Mineralogy and Petrology, v. 155, p. 257-269.

Nash, W. P., and Crecraft, H. R., 1985, Partition coefficients for trace elements in silicic magmas. Geochimica et Cosmochimica Acta, v. 49, p. 2309-2322.

Naumann, T.R., and Geist, D.J., 1999, Generation of alkalic basalt by crystal fractionation of tholeiitic magma: Geology, v. 27, p. 423–426.

Paton, C., Hellstrom, J., Paul, B.,Woodhead, J. and Hergt, J. (2011) Iolite: Freeware for the visualisation and processing of mass spectrometric data. Journal of Analytical Atomic Spectrometry. doi:10.1039/c1ja10172b.

Petrelli, M., Laeger, K., Perugini, D., 2016, High spatial resolution trace element determination of geological samples by laser ablation quadrupole plasma mass spectrometry: implications for glass analysis in volcanic products. Geosciences Journal, 20, 851-863.

Satish-Kumar, M., Hermann, J., Tsunogae, T., and Osanai, Y., 2006, Carbonation of Cl-rich scapolite boudins in Skallen, East Antarctica: evidence for changing fluid condition in the continental crust. Journal of Metamorphic Geology, v. 24, p. 241-261.

Sawyer, E. W., 2008, Atlas of migmatites (Vol. 9). NRC Research press.

Shiraishi, K., Hiroi, Y., Ellis, D. J., Fanning, C. M., Motoyoshi, Y., and Nakai, Y., 1992, The first report of a Cambrian orogenic belt in East Antarctica—an ion microprobe study of the Lützow-Holm Complex. Recent Progress in Antarctic Earth Science, p. 67-73.

Shiraishi, K., Ellis, D. J., Hiroi, Y., Fanning, C. M., Motoyoshi, Y., and Nakai, Y., 1994, Cambrian orogenic belt in East Antarctica and Sri Lanka: implications for Gondwana assembly. The Journal of Geology, v. 102, p. 47-65.

Suzuki, K., and Kawakami, T., 2019, Metamorphic pressure-temperature conditions of the Lützow-Holm Complex of East Antarctica deduced from Zr-in-rutile geothermometer and Al_2SiO_5

minerals enclosed in garnet. Journal of Mineralogical and Petrological Sciences, v. 114, https://doi.org/10.2465/jmps.190801

Tajčmanová, L., Connolly, J. A. D., and Cesare, B., 2009, A thermodynamic model for titanium and ferric iron solution in biotite. Journal of Metamorphic Geology, v. 27, p. 153-165.

Thomas, R., Kamenetsky, V. S., and Davidson, P., 2006, Laser Raman spectroscopic measurements of water in unexposed glass inclusions. American Mineralogist, v. 91, p. 467-470.

Thompson, J. B., and Hovis, G. L., 1979, Entropy of mixing in sanidine. American mineralogist, v. 64, p. 57-65.

Watson, E.B., and Harrison, T.M., 1983, Zircon saturation revisited: temperature and composition effects in a variety of crustal magma types: Earth and Planetary Science Letters, v. 64, p. 295-304.

Wheller, C. J., and Powell, R., 2014, A new thermodynamic model for sapphirine: calculated phase equilibria in K2O–FeO–MgO–Al2O3–SiO2–H2O–TiO2–Fe2O3. Journal of Metamorphic Geology, v. 32, p. 287-299.

White, R. W., Powell, R., and Holland, T. J. B., 2007, Progress relating to calculation of partial melting equilibria for metapelites. Journal of metamorphic Geology, v. 25, p. 511-527

White, R. W., Powell, R., Holland, T. J. B., Johnson, T. E., and Green, E. C. R., 2014, New mineral activity–composition relations for thermodynamic calculations in metapelitic systems. Journal of Metamorphic Geology, v. 32, p. 261-286.

White, R. W., Powell, R., and, Johnson, T. E., 2014, The effect of Mn on mineral stability in metapelites revisited: New a–x relations for manganese-bearing minerals. Journal of Metamorphic Geology, v. 32, p. 809-828.

White, R. W., Powell, R., Holland, T. J. B., and Worley, B. A., 2000, The effect of TiO2 and Fe2O3 on metapelitic assemblages at greenschist and amphibolite facies conditions: mineral equilibria calculations in the system K2O-FeO-MgO-Al2O3-SiO2-H2O-TiO2-Fe2O3. Journal of Metamorphic Geology, v. 18, p. 497-511.

Yoshimura, Y., Motoyoshi, Y., and, Miyamoto, T., 2008. Sapphirine+ quartz association in garnet: implication for ultrahigh-temperature metamorphism at Rundvågshetta, Lützow-Holm Complex, East Antarctica. Geological Society, London, Special Publications, v. 308, p. 377-390.

(a)

Standard glasses
50s acquisition time
5 accumulations

LBG
Sand
Core
B (anhydrous)

3100 3200 3300 3400 3500 3600 3700 3800

Raman shift (cm-1)

(b)

LGB (9.6111±0.4427)
Sand (6.4886±0.4321)
Core (5.7797±0.5457)
B (anhydrous)

Y= 0.0039X - 0.2201
R^2= 0.9826

H2O (wt.%)
0 2 4 6 8 10 12
0 1000 2000 3000
Intensity

(c)

Sand (6.4886±0.4321)
Core (5.7797±0.5457)
B (anhydrous)

Y= 0.0035X - 0.0023
R^2= 0.99997

H2O (wt.%)
0 2 4 6 8
0 1000 2000 3000
Intensity

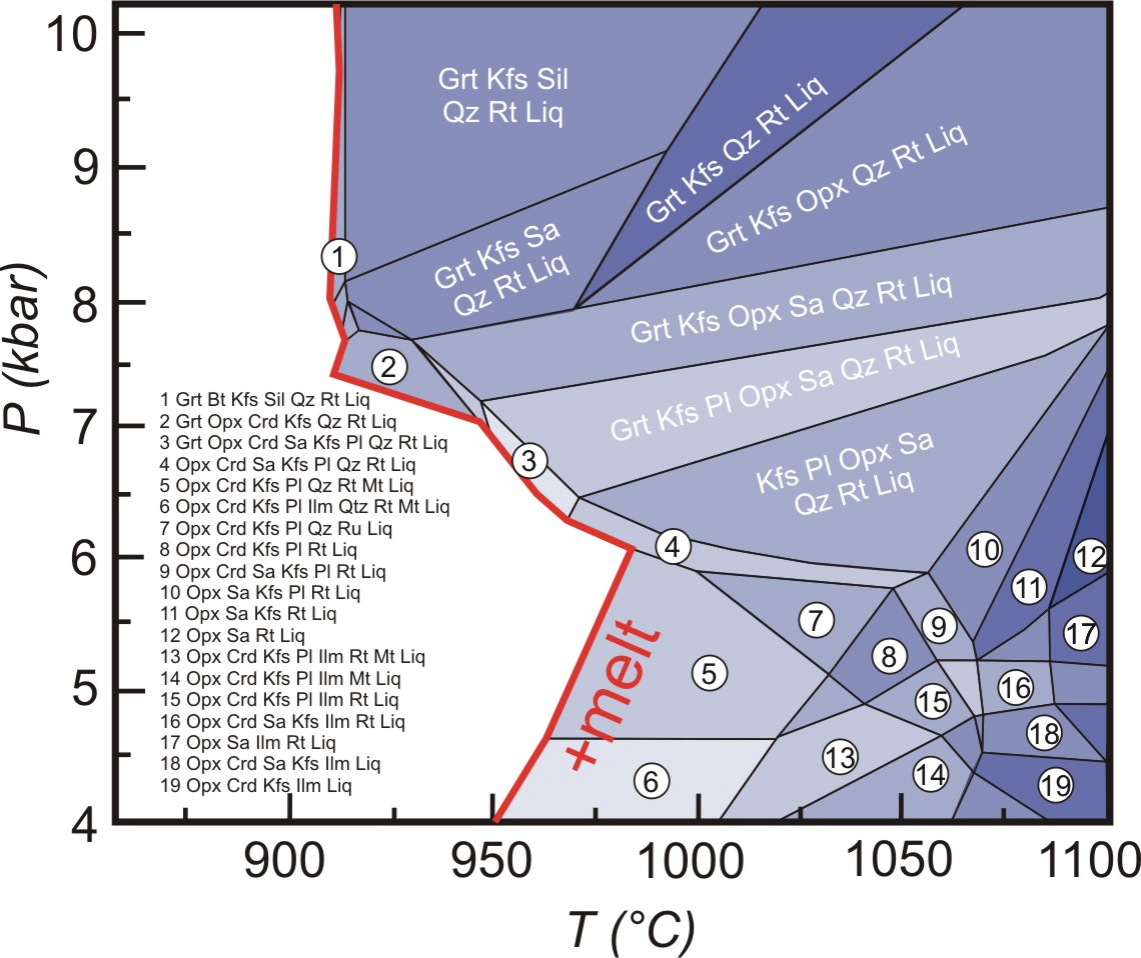
Grt Kfs Sil
Qz Rt Liq
Grt Kfs Qz Rt Liq
Grt Kfs Opx Qz Rt Liq
Grt Kfs Sa
Qz Rt Liq
Grt Kfs Opx Sa Qz Rt Liq
Grt Kfs Pl Opx Sa Qz Rt Liq
Kfs Pl Opx Sa
Qz Rt Liq
+melt
1 Grt Bt Kfs Sil Qz Rt Liq
2 Grt Opx Crd Kfs Qz Rt Liq
3 Grt Opx Crd Sa Kfs Pl Qz Rt Liq
4 Opx Crd Sa Kfs Pl Qz Rt Liq
5 Opx Crd Kfs Pl Qz Rt Mt Liq
6 Opx Crd Kfs Pl Ilm Qtz Rt Mt Liq
7 Opx Crd Kfs Pl Qz Ru Liq
8 Opx Crd Kfs Pl Rt Liq
9 Opx Crd Sa Kfs Pl Rt Liq
10 Opx Sa Kfs Pl Rt Liq
11 Opx Sa Kfs Rt Liq
12 Opx Sa Rt Liq
13 Opx Crd Kfs Pl Ilm Rt Mt Liq
14 Opx Crd Kfs Pl Ilm Mt Liq
15 Opx Crd Kfs Pl Ilm Rt Liq
16 Opx Crd Sa Kfs Ilm Rt Liq
17 Opx Sa Ilm Rt Liq
18 Opx Crd Sa Kfs Ilm Liq
19 Opx Crd Kfs Ilm Liq
P (kbar)
10
9
8
7
6
5
4
900
950
1000
1050
1100
T (°C)